Energy dependence of multipole strength distributions in the $^{32}S(n,p)^{32}P$ reaction

B. K. Park
Ohio University, Athens, Ohio 45701
and New Mexico State University, Las Cruces, New Mexico 88003

J. Rapaport and G. Fink*
Ohio University, Athens, Ohio 45701

J. L. Ullmann, A. G. Ling,† and D. S. Sorenson
Los Alamos National Laboratory, Los Alamos, New Mexico 87545

F. P. Brady and J. L. Romero
University of California, Davis, Davis, California 95616

C. R. Howell and W. Tornow
Duke University and Triangle Universities Nuclear Laboratory, Durham, North Carolina 27706

W. Unkelbach
Indiana University Nuclear Theory Center, Bloomington, Indiana 47408
(Received 5 March 1993)

Double differential cross-section angular distributions were measured for the $^{32}S(n,p)^{32}P$ charge exchange reaction in the $0° \leq \theta_{lab} \leq 14°$ angular range. All data presented here were measured simultaneously covering incident neutron energies between 60 and 220 MeV using the white neutron source at Los Alamos Meson Physics Facility–Weapons Neutron Research. The Gamow-Teller strengths obtained from a multipole decomposition analysis of these $^{32}S(n,p)^{32}P$ data are compared to previously reported $^{32}S(p,n)^{32}Cl$ results as well as to calculated Gamow-Teller strengths obtained using the shell-model code OXBASH and random phase approximation (RPA) calculations. The resultant giant dipole and giant spin-dipole cross sections obtained from this multipole decomposition analysis are also compared with distorted-wave impulse approximations calculated with densities obtained from a simple one-particle–one-hole shell model and also densities obtained from RPA calculations.

PACS number(s): 25.40.Kv, 27.30.+t

I. INTRODUCTION

Notable accomplishments involving charge exchange reactions have been made in recent years on both experimental and theoretical fronts; one such example is found in the case of Gamow-Teller (GT) ($\Delta L = 0, \Delta S = 1, \Delta J^{\pi} = 1^{+}$) transitions. Our present knowledge of GT strength distributions in nuclei came primarily from nucleon scattering data. Beta decay, because of kinematics, probes the GT strength only within a narrow excitation energy window, and therefore misses a large fraction of the GT strength. These GT transitions have been mainly observed with nucleon charge exchange scattering reactions. In these reactions the GT transitions dominate the observed excitation energy spectra at small momentum transfer (q) and at low energy loss (ω). The empirical observation of the giant Gamow-Teller resonance (GGTR) [1–4] and the strong consistency shown between the $L = 0$ zero-degree differential cross section and β-decay strength in both (p,n) and (n,p) reactions [3–6] have sparked a keen interest in the spin-isospin response functions of nuclei.

The $^{32}S(p,n)^{32}Cl$ reaction was studied by Anderson *et al.* [7] using 135 MeV protons with an overall energy resolution of about 270 keV. The deduced GT strength distribution up to about 10 MeV excitation energy is described well by distorted-wave impulse-approximation (DWIA) calculations using full s-d shell-model wave functions with a normalization factor of 0.6. In Sec. III we present a detailed comparison of these (p,n) results and the present (n,p) analysis. With the white neutron source at Los Alamos Meson Physics Facility–Weapons Neutron Research (LAMPF-WNR), we carried out the

*Present address: Eugen-Richter-Str. 159, D-7500 Karlsruhe 21, Germany.
†Present address: TRIUMF, 4004 Wesbrook Mall, Vancouver, British Columbia, Canada V6T 2A3.

studies of (n,p) charge exchange reactions covering the incident neutron energies between 60 and 220 MeV simultaneously. Furthermore, concurrent scattering angle measurements were produced covering $0° \leq \theta_{\rm lab} \leq 14°$. These simultaneous measurements of the double differential cross-section angular distribution render studies of energy dependent quantities most suitable.

For nuclei with the same number of neutrons and protons ($T = 0$) such as ^{32}S, both (p,n) and (n,p) reactions excite similar $T = 1$ states. Therefore (n,p) studies on the ^{32}S nucleus are complementary to previous (p,n) studies. One advantage of using the ^{32}S$(n,p)^{32}$P reaction over the ^{32}S$(p,n)^{32}$Cl reaction as an isovector probe is that it has a lower ground state Q value of -0.93 MeV as compared to -13.5 MeV for the latter reaction. Consequently, (n,p) studies provide data much closer to q near 0, a feature particularly important in identifying GT transitions. Furthermore, the three-body breakup threshold is at a higher excitation energy in the ^{32}P residual nucleus ($\sim$ 8 MeV) than in the ^{32}Cl nucleus ($\sim$ 0.5 MeV). In general, this allows for (n,p) studies to obtain excitations of giant resonances with less contributions from the "continuum" due to the three-body breakup.

In this paper we report on the GT strength observed in the ^{32}S$(n,p)^{32}$P reaction by mapping its distribution both as a function of excitation energy in ^{32}P and of the incident nucleon energy. A multipole decomposition (MD) analysis [8,9] was done to obtain additional multipole contributions that form the excitation spectra up to 35 MeV. This analysis requires DWIA calculations, which were done with the program DW81 [10] using a full microscopic model for the ^{32}S$(n,p)^{32}$P reaction. The extracted GT strengths in the ^{32}S$(n,p)^{32}$P reaction are compared with those from the ^{32}S$(p,n)^{32}$Cl measurements [7] and the OXBASH [11] shell-model calculations. In the shell model, the ground state of a nucleus can be represented by filling up all single-particle states up to the Fermi level. These single-particle states are obtained as solutions of a mean field potential (Woods-Saxon or Hartree-Fock). Neglecting a residual interaction between the nucleons, the lowest excited states can be considered as simple one-particle–one-hole ($1p$-$1h$) configurations. We get a a glimpse of what takes place in nuclear reactions using these $1p$-$1h$ configurations in the simple shell model. For a more realistic description of the data, we have performed random phase approximation (RPA) DWIA calculations of the differential cross section to compare with experimental data. In the RPA we take into account the residual interaction between the nucleons. The excited states are described as superposition of p-h states, which gives a more realistic description of the excited states. A brief summary of the RPA-DWIA calculation is included in Sec. III. For a more detailed description of RPA, see Ref. [12].

At high excitation energy ($E_x \geq$ 10–15 MeV) and beyond the main region of giant Gamow-Teller resonance (GGTR) region, it is difficult to infer possible $L = 0$ transitions due to the presence of strong $L = 1$ excitations. Although there exists a few MeV energy separation between the centroids of the GT and the $L = 1$ excitations, a good portion of the lower part of the excitation energy region in ^{32}P ($E_x \leq 20$ MeV) may be shared by both. Therefore, an accurate account of the $L = 1$ excitation will undoubtedly improve the quality of extracting the empirical GT strength and vice versa.

Giant resonances may be interpreted as the collective motion of nucleons in the nucleus in a narrow band of excitation energies where most of the transition strengths for a given set of quantum numbers is deposited. From the nuclear structure point of view, there has been considerable interest in the study of relative locations of the giant dipole resonance (GDR) ($\Delta L = 1, \Delta S = 0, \Delta J^\pi = 1^-$) and giant spin-dipole resonance (GSDR) ($\Delta L = 1$, $\Delta S = 1, \Delta J^\pi = 0^-, 1^-, 2^-$) [13]. Up to $E_n \approx 200$ MeV, the relative magnitude of the isospin (v_τ) part decreases with increasing energy with respect to the spin-isospin ($v_{\sigma\tau}$) part of the isovector effective interaction [14]. Thus, the GDR should be excited more strongly at lower incident energies ($E \leq 100$ MeV) while the GSDR should be excited more strongly at higher energies ($E \geq 150$ MeV). The present data from LAMPF-WNR provide a unique opportunity to study the energy-dependent behavior of the nuclear force at a momentum transfer q $\sim$ 0.5 fm^{-1}, corresponding to the peak of the $L = 1$ angular distribution. This complements similar studies at $q = 0$ fm^{-1} done for GT transitions [15].

II. EXPERIMENT

The white neutron source at the Weapons Neutron Research center at Los Alamos National Laboratory (LAMPF-WNR) [16] was used to provide simultaneously neutrons in the energy range between 60 and 220 MeV. Our experimental setup was located approximately 90 m away from the neutron production target and 15° left of the proton beam line. With 90 m flight path, an energy resolution ranging from 1.0 to 3.0 MeV was achieved. A more complete description of this facility may be found in Refs. [9, 17, 18]. We present here just a brief description of the present setup.

The neutron beam, collimated to a size of 10 × 10 cm^2, entered the detector hut and passed through two charged-particle veto chambers. Any incoming charged particles produced in the neutron flight path were eliminated in software. The veto and target chambers were single-plane multiwire proportional chambers. Targets were positioned in a multitarget array (four combinations of target and target chambers) similar to the one described by Henderson *et al.* [19]. Target chambers were used for tagging individual events to identify the origin of these events. Targets of $^{\rm nat}$Ca (200 mg/cm^2, 97% ^{40}Ca, 12.5 × 12.5 cm^2) [20], ^{60,64}Ni [each 150 mg/cm^2, 7.5 × 5 cm^2; ^{60}Ni (^{64}Ni) was placed on the top (bottom) half] [21], $^{\rm nat}$S (200 mg/cm^2, 95% ^{32}S, 12.0 × 12.0 cm^2), and CH_2 (76.1 mg/cm^2, 12.0 × 12.0 cm^2) were placed in target positions 1–4, respectively. A gas mixture of 70% argon, 30% CO_2, and 0.2% freon [17] was used to fill the veto and target chambers, to reduce the hydrogen background contributions. The sulfur target was enclosed by 0.0064-mm-thick Mylar windows. A CH_2 target was placed in the fourth target position throughout the exper-

iment to obtain the yield from the ^{1}H(n,p) reaction for normalization. Values for the ^{1}H(n,p) cross section were obtained from the SM88 phase-shift solution of Arndt *et al.* [22]. The trajectories and scattering angle of protons leading to the CsI calorimetry detectors were determined using four drift chambers that were filled with a gas mixture of 65% argon and 35% isobutane. A dipole magnet (0.5 T), situated between two pairs of the drift chambers, was used to deflect the trajectories of forward-scattered protons out of the neutron beam and into the detector array. A large plastic ΔE scintillator ($30.5 \times 50.8 \times 0.5$ cm^3) was positioned in front of the CsI (Tl) detectors to determine the incident neutron energies using the time-of-flight technique as well as to provide particle identifications. The energy of detected protons was measured with 15 CsI crystals (each $8.9 \times 8.9 \times 15.2$ cm^3) that were stacked up in an array of three rows and five columns. This detection system could simultaneously measure proton scattering angles from $\theta_{\rm lab} = 0°$ to 14° with a total solid angle of 50 msr. In the present experiment, we have the solid angle that depends on both the target position and proton energy due to the multitarget array and a dipole magnet, respectively. Additional information on the present setup including detailed discussion of the solid angle can be found in Refs. [9, 17, 18]. A schematic drawing of the setup can be found in Refs. [9, 18, 20, 21].

Neutron fluxes incident on the target were of the order of a few thousand neutrons per second per MeV [9]. Although the running time was a few weeks, we had to increase the yield statistics by binning the data in neutron energy intervals $\Delta E_n = 10$ MeV for incident neutron energies E_n below 100 MeV and 20 MeV intervals for E_n above 100 MeV. In addition, a 2° angle binning was used. For example, the notation $\theta_{\rm lab} = 5°$,

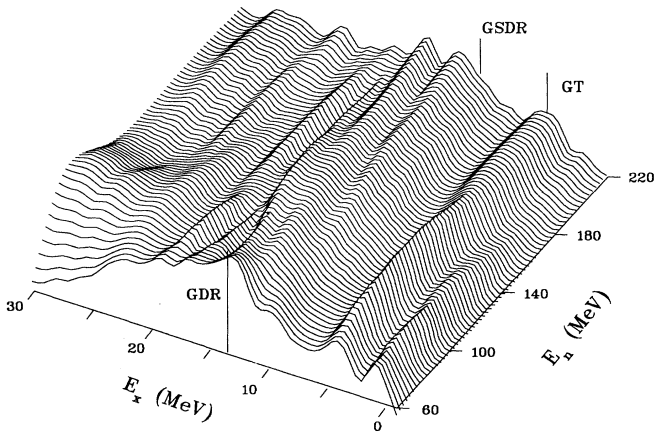

FIG. 1. Three-dimensional plot of $(E_x, E_n, d^2\sigma/d\Omega dE)$ for the ^{32}S$(n,p)^{32}$P data at $\theta_{\rm lab} = 7°$ covering neutron energies between 60 and 220 MeV. The cross section for the GSDR in the lower part of the $L = 1$ dipole resonance increases with E_n. The giant Gamow-Teller resonance is very prominent at about $E_x = 4.5$ MeV.

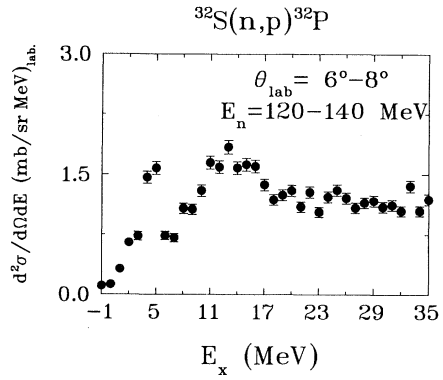

FIG. 2. Cut in the 3D plot of Fig. 1 at $E_n = 130$ MeV and $\theta_{\rm lab} = 7°$. An overall energy resolution of about 1.3 MeV was achieved.

130-MeV ^{32}S$(n,p)^{32}$P data represents the data between $120 \le E_n \le 140$ MeV and $4° \le \theta_{\rm lab} \le 6°$.

A sample of the data is presented in Fig. 1 in the form of a three-dimensional (3D) plot observed at $\theta_{\rm lab} = 7°$ for the ^{32}S$(n,p)^{32}$P reaction. The double differential cross section for an excitation energy region up to 30 MeV is displayed as a function of incident neutron energy in the 60–220 MeV range. The uniqueness of the white neutron source is very well represented in this figure. In a monoenergetic experiment, one would measure only one of the curves shown in this figure. It is only at WNR with the white neutron source that the energy dependence can be studied simultaneously. A typical spectrum, corresponding to a cut in the 3D plot at $E_n = 130$ MeV, is shown in Fig. 2. An overall proton energy resolution of about 1% of the incident neutron energy was achieved in the present experiment.

III. DISCUSSION

The measured spectra at low momentum transfer and low energy loss are rich in information about the energy dependence of giant isovector resonances, in particular the GGTR, GDR, and GSDR. The separation of these resonances using the energy dependence is one of the main objectives of the present experiment. The energy resolution from this type of experiments is not good enough to separate individual states. Thus we decided to do a multipole decomposition (MD) analysis at several incident neutron energies. In particular, we performed a MD analysis at $E_n = 130$ MeV to compare with the GT analysis reported in Ref. [7] for the ^{32}S$(p,n)^{32}$Cl reaction at $E_p = 135$ MeV. In addition, we present MD analyses done at $E_n = 95$ and 170 MeV to study the energy dependence of both the GT strength and $L = 1$ transition. Similar to the MD analysis presented in Ref. [20], the center-of-mass double differential cross-section data were binned in 1-MeV excitation energy intervals. The choice of 1-MeV excitation energy bins was made to have the bin size smaller than the experimental energy resolution in order to distinguish the peaks of in-

TABLE I. Particle-hole configurations used in the multipole decomposition analysis for the ^{32}S$(n,p)^{32}$P data.

J^π	p-h	J^π	p-h
0^-	$1f_{5/2}1d_{5/2}^{-1}$	2^+	$1d_{3/2}1d_{5/2}^{-1}$
1^-	$1f_{5/2}1d_{5/2}^{-1}$	3^-	$1f_{5/2}1d_{5/2}^{-1}$
1^+	$1d_{3/2}1d_{5/2}^{-1}$	3^+	$1d_{3/2}1d_{5/2}^{-1}$
2^-	$1f_{5/2}1d_{5/2}^{-1}$	4^-	$1f_{5/2}1d_{5/2}^{-1}$

terest. Calculated DWIA angular distribution shapes for different ΔJ^π transfers were then fitted to the measured angular distributions. The shape of $\sigma(\theta)$ changes smoothly with increasing excitation energy E_x. Therefore, these calculations were done at 5-MeV excitation energy intervals. A subroutine was used to interpolate in 1-MeV excitation energy intervals and the fitting to the data was done using a least-squares technique [23]. Since the angular distributions were limited to $\theta_{\rm lab} \leq 14°$, we assume transitions characterized by just the following ΔJ^π transfers: $1^+, 0^-, 1^-, 2^-, 2^+, 3^+, 3^-$, and 4^- (see Table I). We used the shell-model code OXBASH [11] to help identify the most probable $1p$-$1h$ configurations as a function of excitation energy in ^{32}P [9]. Upon carrying out DWIA calculations for each value of ΔJ^π, for the different transition amplitudes resulting from the shell-model calculations, it was realized that the DWIA shapes were generally characteristic of the value of ΔJ^π. Therefore, we used a $1p$-$1h$ configuration that is representative of transition amplitudes for each value of ΔJ^π. These are listed in Table I. Except for the 1^+ transitions, these configurations are similar to those described in the analysis of the ^{40}Ca$(n,p)^{40}$K data [20]. We employed the code DW81 to perform the distorted-wave impulse-approximation calculations. The DW81 calculations require knowledge of the nucleon-nucleus mean field, the nucleon-nucleon (NN) interaction, and the transition density-matrix elements. For the nucleon-nucleus mean field, we used optical potential parameters obtained by Schwandt *et al.* [24] in the phenomenological global optical-model analysis of elastic scattering proton data in the E_p = 80–180 MeV range and $24 \leq A \leq 208$. For the effective interaction, the free NN t matrices parametrized by Franey and Love [14] were used. The transition densities were computed assuming harmonic oscillator single-particle wave functions with an oscillator parameter b = 1.88 fm [25].

The cross-section distribution for GT transitions were calculated using the one-body density-matrix elements (OBDME) calculated by Brown and Wildenthal [26]. We used the shell-model code OXBASH to generate OBDME for $1p$-$1h$ transitions in a rather simple SDPF shell-model space for dipole and spin-dipole final states [9]. The shell-model space includes $1d_{5/2}, 1d_{3/2}, 2s_{1/2}$ holes and $1f_{7/2}, 1f_{5/2}, 2p_{3/2}, 2p_{1/2}$ particles assuming $1\hbar\omega$ excitations. The transition densities were obtained from the calculated wave functions using the Millener-Kurath [27] form for the residual interaction.

We also present calculations done in the random phase approximation (RPA) DWIA method. The nuclear structure is described in terms of the RPA. Transitions between the ground state of the ^{32}S nucleus and final states in the ^{32}P are treated as a coherent sum of particle-hole excitations. Transition densities obtained from this calculation, folded with the effective projectile-target interaction, give form factors as a starting point for a distorted-wave calculation. A detailed description of the formalism can be found in Ref. [28]. The single-particle space for the RPA is determined by a Woods-Saxon calculation using the parameters of Table II which were chosen to reproduce optimally the single-particle spectrum close to the Fermi surface. The wave functions have been expanded in terms of harmonic oscillators, and so a discretized continuum has been obtained. All states up to 50 MeV in the continuum are taken into account. Near the Fermi surface, single-particle energies were taken from experimental data [29, 30]. For the residual interaction a Landau-Migdal force [31]

$$\hat{v}_{\rm res}(\mathbf{r},\mathbf{r}') = C_0\delta(\mathbf{r}-\mathbf{r}')[f_0' + g_0'\boldsymbol{\sigma}\cdot\boldsymbol{\sigma}']\boldsymbol{\tau}\cdot\boldsymbol{\tau}', \qquad (1)$$

with parameters

$$C_0 = 300\,{\rm MeV\,fm^3}, \quad f_0' = 1.5, \quad g_0' = 1.0, \qquad (2)$$

has been used, in order to reproduce the low energy spectrum in ^{32}S. The effective projectile-target interaction is described by the free NN t matrix of Franey and Love [14]. The DWIA calculations were done using the computer code DWUCK4 [32]. The incoming and outgoing distorted waves are calculated using the optical-model potential parameters of Schwandt *et al.* [24]. The spreading

TABLE II. Optical-model potential[a] parameters for ^{32}S.

^{32}S	V_0 (MeV)	R (fm)	a (fm)	$V_{\rm LS}$ (MeV)	$R_{\rm LS}$ (fm)	$a_{\rm LS}$ (fm)	R_C (fm)
p	−61.4	3.70	0.80	9.95	3.84	0.53	3.70
n	−60.3	3.70	0.80	9.77	3.84	0.53	

[a]The optical potential is parameterized as

$$U(r) = U_{\rm Coul}(r) - Vf_{v0}(r) - iWf_w(r) + \frac{2}{r}\left[V_{\rm SO}\frac{d}{dr}f_{v\rm SO}(r) + iW_{\rm SO}\frac{d}{dr}f_{w\rm SO}(r)\right]\mathbf{L}\cdot\boldsymbol{\sigma},$$

with the Woods-Saxon form factor

$$f(r) = \frac{1}{1+e^{(r-R/a)}}, \quad R = r_o A^{1/3}.$$

widths $\Gamma\downarrow$ due to $2p$-$2h$ damping in the continuum have been taken into account in an approximate way by folding in a Breit-Wigner distribution with an energy-dependent width [33]. In the calculation all multipolarities up to $J = 5$ have been summed up to ensure convergence.

A. Multipole decomposition analysis

The shapes of the calculated angular distributions are characterized by ΔJ^π transfers. However, the differences in shapes among the members of a given ΔL transfer are not large enough to determine individual ΔJ^π ($\Delta\mathbf{J} = \Delta\mathbf{L} + \Delta\mathbf{S}$) contributions from the present experimental data. Therefore, we choose to report the results of the MD analysis by grouping all ΔJ^π transitions that correspond to a given ΔL transfer. As such, we assume $\Delta L = 0$ for the $\Delta J^\pi = 1^+$ transition, $\Delta L = 1$ for $\Delta J^\pi = 0^-, 1^-$, and 2^- transitions, $\Delta L = 2$ for $\Delta J^\pi = 2^+$ and 3^+ transitions, and $\Delta L = 3$ for $\Delta J^\pi = 3^-$ and 4^- transitions.

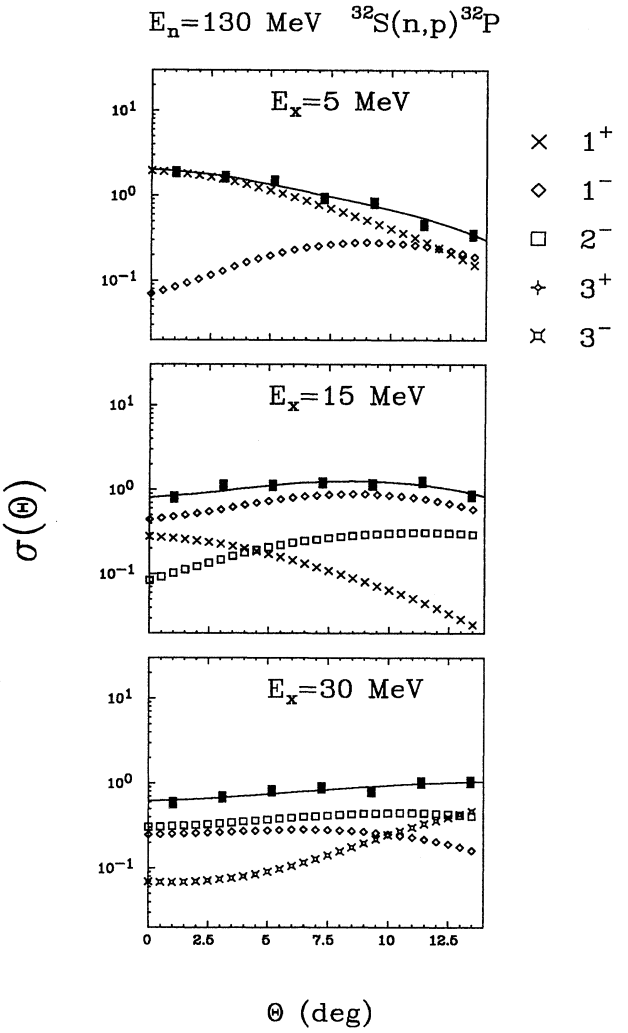

FIG. 3. Individual and sum of the calculated and weighted angular distributions $\alpha_{J^\pi}\sigma(\theta)^{\mathrm{DW81}}_{J^\pi}$ at $E_x = 5$, 10, and 15 MeV for the 130-MeV $^{32}\mathrm{S}(n,p)^{32}\mathrm{P}$ reaction. In all three cases, the sum of the calculated and weighted cross sections, which is represented by a solid line, agrees well with the observed cross sections (solid squares). The strength of each $\sigma(\theta)^{J^\pi}$ has been determined from the MD analysis. At $E_x = 5$ MeV we *observe* mostly $\sigma(\theta)^{J^\pi}$ of $J^\pi = 1^+(L = 0)$. The angular distribution at $E_x = 10$ and 15 MeV are mainly composed of $\sigma(\theta)^{J^\pi}$ of $J^\pi = 1^-$ and 2^- $(L = 1)$.

In performing the MD analysis, the observed angular distribution for each excitation energy bin was used in the fitting routine. In the present study, cross sections between 0° and 14° were binned in 2° steps to provide 7 angles. Ideally, one would like to deduce the strength distribution of each ΔJ^π transitions listed above. However, χ^2 procedures limit the number of free parameters in fitting seven independent cross-section values. Therefore, in the present MD analysis, we used a set of five α_{J^π} fitting coefficients to describe the experimental data with the following expression:

$$\left(\frac{d\sigma(\theta)}{d\Omega}\right)_{\mathrm{data}} \equiv \sigma(\theta)_{\mathrm{data}} = \sum_{J^\pi} \alpha_{J^\pi}\sigma^{\mathrm{DW81}}_{J^\pi}(\theta). \qquad (3)$$

For each 1-MeV excitation energy interval, results of doing a least-squares fit with different combinations of $\sigma^{\mathrm{DW81}}_{J^\pi}(\theta)$ were stored and the set of positive coefficients giving the minimum error was chosen. In Eq. (3) $\sigma^{\mathrm{DW81}}_{J^\pi}(\theta)$ represents shapes of the DWIA calculations. The positive coefficients ensure that we have positive cross sections. In Fig. 3 we show the calculated angular distributions $\sigma^{\mathrm{DW81}}_{J^\pi}(\theta)$ at $E_x = 5$, 10, and 15 MeV for the $^{32}\mathrm{S}(n,p)^{32}\mathrm{P}$ reaction obtained at $E_n = 130$ MeV. In all three cases, the sum of the weighted $\sigma^{\mathrm{DW81}}_{J^\pi}(\theta)$'s from the MD analysis represented by a solid line agrees well with the observed cross sections (solid squares). At $E_x = 5$ MeV we observe mostly $\sigma(\theta)^{J^\pi}$ with $J^\pi = 1^+$ $(L = 0)$. The angular distributions at $E_x = 10$ and 15 MeV are mainly composed of transitions with $J^\pi = 1^-$ and 2^- $(L = 1)$.

B. Multipole decomposed $^{32}\mathrm{S}(n,p)^{32}\mathrm{P}$ data

In Figs. 4, 5, and 6, the multipole decomposed spectra are shown for the 95-, 130-, and 170-MeV $^{32}\mathrm{S}(n,p)^{32}\mathrm{P}$ reaction. In these figures, we have displayed $\sigma(\theta)^{\mathrm{DW81}}_{L}$ [sum of appropriate $\sigma(\theta)^{\mathrm{DW81}}_{J^\pi}$'s weighted with α_{J^π} coefficients] and overlaid on the (n,p) data. Only the statistical uncertainties of the measured cross sections are shown. As can be seen in these figures, the agreement between the $\sigma(\theta)_{\mathrm{data}}$ and $\sum\sigma(\theta)^{\mathrm{DW81}}_{L}$ is excellent for all three cases. The excitation spectra ($E_x \leq 35$ MeV) were decomposed using five $\sigma(\theta)^{\mathrm{DW81}}_{J^\pi}$ shapes to represent $L = 0$, 1, 2, and 3 transfers (see Table I). The choices of $\sigma(\theta)^{\mathrm{DW81}}_{J^\pi}$ to describe the $\sigma(\theta)_{\mathrm{data}}$ were mainly based on selecting the combination that results in the smallest overall χ^2 error. For the 95- and 130-MeV $^{32}\mathrm{S}(n,p)^{32}\mathrm{P}$ data, both $\sigma(\theta)^{\mathrm{DW81}}_{J^\pi}$ for $J^\pi = 1^+, 0^-, 1^-, 2^-, 3^+$ and $\sigma(\theta)^{\mathrm{DW81}}_{J^\pi}$ for $J^\pi = 1^+, 1^-, 2^-, 3^+, 3^-$ seem to describe the $\sigma(\theta)_{\mathrm{data}}$ equally well for all possible combinations that were tested. For the 170-MeV $^{32}\mathrm{S}(n,p)^{32}\mathrm{P}$ data, we needed to introduce the $\sigma(\theta)^{J^\pi}$ of $J^\pi = 3^-$ for $L = 3$ transfer in place of 0^- for $L = 1$ transfer to *match* the

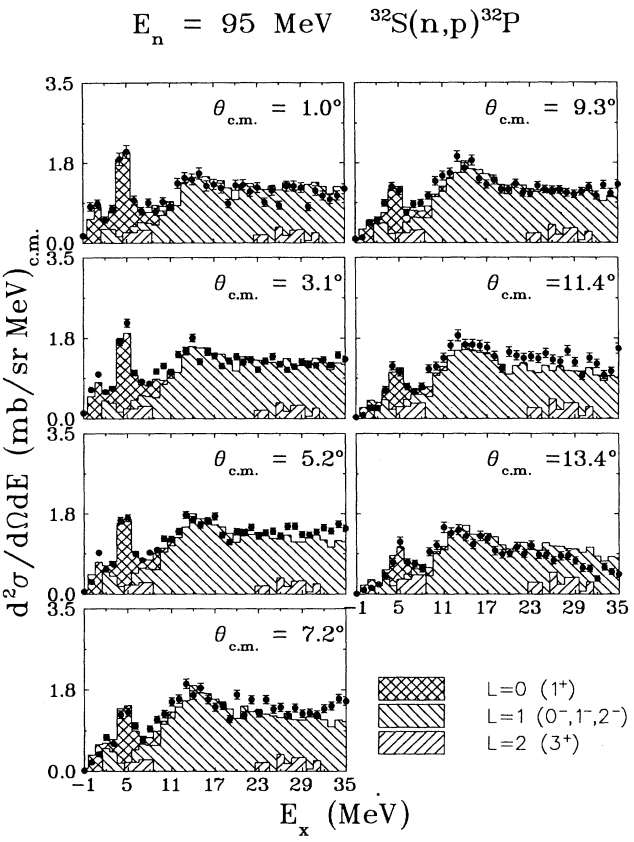

FIG. 4. Multipole decomposed spectra for the 95-MeV ^{32}S$(n,p)^{32}$P reaction at the indicated angles. Experimentally observed cross sections are displayed with error bars representing the statistical uncertainties. Cross sections characterizing the L transfers 0, 1, 2, and 3 are shown.

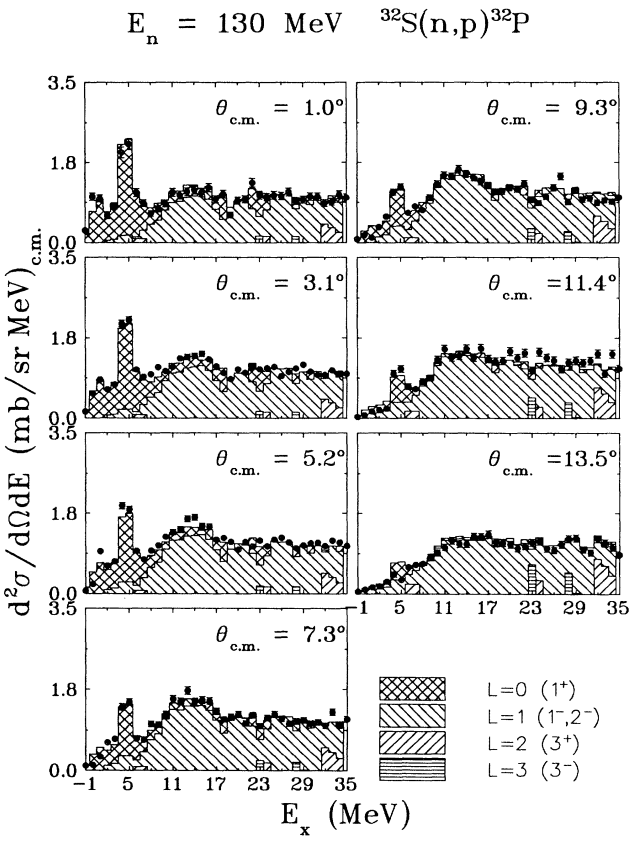

FIG. 5. Same as in Fig. 4 but at E_n = 130 MeV at the indicated angles. Observed excitation spectra are decomposed using calculated cross sections of L transfers 0, 1, 2, and 3.

data at higher excitation energy. The contribution of the $\sigma(\theta)^{J^\pi}$ for $J^\pi = 0^-$ was negligible compared to others at this energy and this was inferred from both DW81 calculation and the multipole decomposed spectra. We point out that our results for the $L = 0$ cross section from the multipole decomposed spectra below $E_x = 10$ MeV were essentially independent of the choices of $\sigma(\theta)^{J^\pi}$ for $L = 1$, 2, or 3 transfers. This suggests a reasonably high accuracy in identifying the $L = 0$ (1^+) cross section below $E_x = 10$ MeV in the ^{32}S$(n,p)^{32}$P data. In all three sets of the multipole decomposed spectra, mostly GT transitions are seen below $E_x = 10$ MeV and the GGTR is very prominent at $E_x = 4.5$ MeV. We will not attempt to distinguish individual $\sigma(\theta)^{J^\pi}$'s that belong to $L = 1$ transfer.

C. GT strength distribution in the ^{32}S$(n,p)^{32}$P reaction

The GT strength distribution may be obtained from the measured $L = 0$ cross sections if the unit GT cross section $\hat{\sigma}_{\rm GT}^{(np)}$ is known [5]. The ^{32}P(g.s.)^{32}S β decay with a known log(ft) value of 7.90 [34] renders an extremely small ^{32}S$(n,p)^{32}$P(g.s.) differential cross section of $\sim 1 \times 10^{-5}$ mb/sr, and therefore it is too weakly excited to be used as a standard reference with which we can calculate the $\hat{\sigma}(A = 32, E_n)$ value. The ^{32}S$(p,n)^{32}$Cl reaction at $E_p = 135$ MeV and $\theta_{\rm lab} = 0.2°$ was studied by Anderson *et al.* [7]. For $T = 0$ nuclei, we expect the same GT strengths in both (n,p) and (p,n) channels [35]. Thus, we present the comparison of the $L = 0$ cross sections obtained from the MD analysis of the present data at 130 MeV and the analysis of the ^{32}S$(p,n)^{32}$Cl at 135 MeV reported by Anderson *et al.* [7]. We also make a comparison with the calculated GT strengths with the RPA and the OXBASH code.

D. Unit Gamow-Teller cross section $\hat{\sigma}_{\rm GT}(A = 32, E_n)$

We use the integrated GT value reported by Anderson *et al.* [7] in the ^{32}S$(p,n)^{32}$Cl reaction at 135 MeV, to normalize the MD-analyzed $L = 0$ cross section extracted from the (n,p) data at 130 MeV. We do this because the different energy resolutions in the two experiments [0.3 MeV in the (p,n) and 1.4 MeV in the (n,p), respectively] do not allow a comparison to an individual transition. A value $\sum_{E_x=0}^{10\ \rm MeV} B({\rm GT}) = 2.212$ is reported for the ^{32}S$(p,n)^{32}$Cl reaction [7] with a sum cross-section value of $\sum_{E_x=0}^{10\ \rm MeV} \sigma_{L=0} = 14.00 \pm 2.10$ mb/sr. Given here is a net uncertainty in the total 1^+ "peak" strength, and

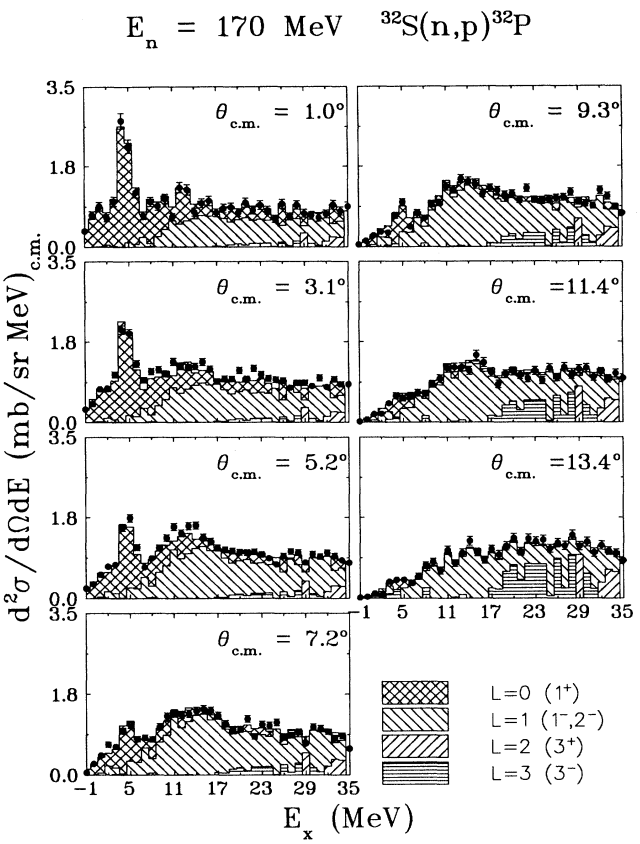

FIG. 6. Same as in Fig. 4 but at E_n = 170 MeV.

includes uncertainties in fitting of GT peaks and in doing the background subtraction. The cross-section values were extrapolated to $\omega = 0$ and $q = 0$ fm^{-1}. Because of the difficulties in identifying GT strengths at higher excitation energy region due to smaller and more-fragmented GT strengths and a rather large uncertainty associated with a choice of background in this region, Anderson *et al.* only considered "peaks" in the (p,n) spectrum. They reported that about 1 ± 2 mb/sr could be considered as GT cross sections between $E_x = 10$ and 20 MeV. A rather large uncertainty is assigned mainly due to assumptions that they made in this estimation. In the following discussion, although we keep this in mind, we choose not to use $\sum_{E_x=10}^{20\ \mathrm{MeV}} \sigma_{L=0}^{pn} = 1 \pm 2$ mb/sr because the uncertainty overshadows any meaningful comparisons.

The MD analysis shows that about 20% of the cross sections observed in $E_x \leq 10$ MeV region is from $L = 1$ dipole excitations. The values $\sum_{E_x=0}^{10\ \mathrm{MeV}} \sigma_{L=0}^{np} = 9.9$ mb/sr and $\sum_{E_x=0}^{10\ \mathrm{MeV}} \sigma_{L=1}^{np} = 2.3$ mb/sr are obtained from the MD-analyzed 130-MeV ^{32}S$(n,p)^{32}$P spectrum at $\theta_{\mathrm{lab}} = 1°$. Extrapolating $\sum_{E_x=0}^{10\ \mathrm{MeV}} \sigma_{L=0}^{np} = 9.9$ mb/sr to $q = 0$, we obtain 11.4 ± 2.0 mb/sr. The uncertainty is obtained by adding in quadrature the statistical uncertainty (~ 2%), a modest 10% uncertainty in the MD analysis, and overall 15% uncertainty in background subtraction and solid angle correction in data reduction. We use a unit GT cross section value of 11.4 mb/sr at 130 MeV divided by 2.212 GT units or $\hat{\sigma}_{\mathrm{GT}}$ $(A = 32, E_n = 130$ MeV) = 5.2 mb/sr unit (GT). The integrated GT value reported by Anderson *et al.* [7] in the ^{32}S$(p,n)^{32}$Cl reaction at 135 MeV is used to normalize the MD-analyzed $L = 0$ cross section extracted in the (n,p) data at 130 MeV.

In order to calculate the values of $\hat{\sigma}_{\mathrm{GT}}$ as a function of E_n, we have used a peak-fitting routine to get the cross section of GT transitions (see inset in Fig. 7). From the knowledge that almost all the differential cross sections below $E_x = 7$ MeV are characterized with $L = 0$ transfer, we have decided to use two Gaussian peaks located below ~7 MeV in excitation energy for all neutron energies. The obtained $\hat{\sigma}_{\mathrm{GT}}$ versus E_n is shown in Fig. 7. A smooth variation of the $\hat{\sigma}_{\mathrm{GT}}$ with respect to E_n is seen in this figure; above $E_n = 100$ MeV almost a linear pattern is observed. We parametrized the following empirical relationship for the energy dependence of the $\hat{\sigma}_{\mathrm{GT}}$:

$$\hat{\sigma}_{\mathrm{GT}}(A = 32, E_n) = 10^{(0.585+0.001E_n)}, \quad (4)$$

where E_n is in MeV. Additional GT strength is seen in the MD-analyzed (n,p) spectra between $E_x = 10$ and 20 MeV. This is true for all three cases that we have tested (see Table III, Figs. 4, 5, and 6). A value $\sum_{E_x=0}^{20\ \mathrm{MeV}} \sigma_{L=0}^{np}$ = 12.1 mb/sr is obtained from the MD-analyzed 130-MeV ^{32}S$(n,p)^{32}$P spectrum at $\theta_{\mathrm{lab}} = 1°$. Extrapolating this cross section to $q = 0$ fm^{-1}, we obtain 13.9 ± 2.3 mb/sr. In Table III we use Eq. (4) to tabulate values for $\sum B(\mathrm{GT})$ at 95, 130, and 170 MeV for the ^{32}S$(n,p)^{32}$P data along with the 135-MeV ^{32}S$(p,n)^{32}$Cl data and results from the OXBASH and RPA calculations at different excitation energy intervals. Although the value for $\sum B(\mathrm{GT})$ is slightly higher at 170 MeV and lower at 95 MeV as compared to the 130-MeV (n,p) data, all values fall within the estimated uncertainties and the overall agreement is quite reasonable. Almost all $\sum B(\mathrm{GT})$ strength that has been observed in the (p,n) study *resides* below $E_x = 10$ MeV. The $\sum B(\mathrm{GT})$ from the OXBASH calculation is in agreement with this observation. However, additional GT strength in the $E_x = 10$ to 20 MeV region is seen in the present (n,p) data as well as from the RPA calculations. Some of this additional strength seen in the (n,p) data may be due in part to

TABLE III. Values of $\sum B(\mathrm{GT})$ tabulated for the ^{32}S$(p,n)^{32}$P data, OXBASH calculation, and ^{32}S$(n,p)^{32}$P data at different excitation energy intervals.

Source	$\sum_{E_x=0}^{10\ \mathrm{MeV}} B(\mathrm{GT})$	$\sum_{E_x=0}^{20\ \mathrm{MeV}} B(\mathrm{GT})$
135 MeV (p,n) [7]	2.21 ± 0.33	
OXBASH [37]	2.02	2.10
RPA	2.14	2.67
95 MeV (n,p)	2.3 ± 0.4	2.4 ± 0.4
130 MeV (n,p)[a]	2.2 ± 0.4	2.7 ± 0.5
170 MeV (n,p)	2.4 ± 0.4	3.0 ± 0.6

[a] $\sum_{E_x=0}^{10\ \mathrm{MeV}} B(\mathrm{GT})$ of the 130-MeV ^{32}S$(n,p)^{32}$P data has been normalized to $\sum_{E_x=0}^{10\ \mathrm{MeV}} B(\mathrm{GT})$ of the 135-MeV ^{32}S$(p,n)^{32}$Cl [7].

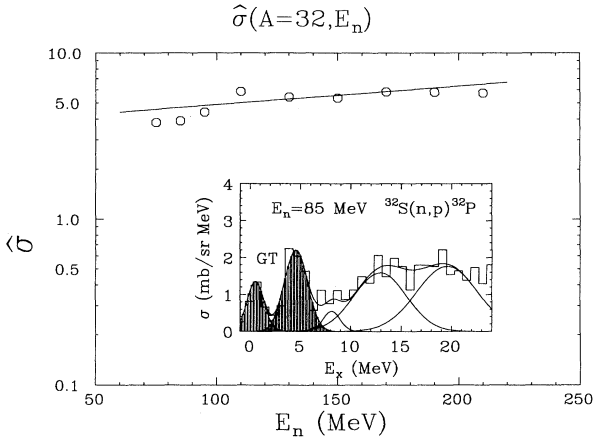

FIG. 7. Unit GT cross sections $\hat{\sigma}(E_n)$ between $E_n = 70$ and 220 MeV obtained for the ^{32}S$(n,p)^{32}$P reaction. The 85-MeV ^{32}S$(n,p)^{32}$P data are at $\theta_{\rm lab} = 1°$ shown in an inset. A total of six Gaussian curves were used to fit the data in the range $0 \leq E_x \leq 25$ MeV. The sum of the areas of the first two Gaussians with centroids at $E_x = 1$ and 4.5 MeV was used to calculate the observed GT cross section.

uncertainties in the assumed shapes for the $L = 1$ and 2 transfers in the MD analysis which have a larger influence on weaker GT transitions in the E_x region above 10 MeV (see Table III.)

Additional information concerning the $\hat{\sigma}(A, E_n)$ for other targets studied using the present experimental setup can be found in Refs. [35, 36]. The angular distribution of $\sum_{E_x=0}^{10\ \rm MeV} \sigma_{L=0}^{MD}(\theta)$ obtained from the multipole decomposed spectra for the 130-MeV ^{32}S$(n,p)^{32}$P data is shown in Fig. 8. The curve shown in this figure is an arbitrarily normalized DW81 calculation for $\sigma(\theta)^{J^\pi}$ for $J^\pi = 1^+$ transition at $E_x = 5$ MeV. A good agreement in shape is found between this curve and the sum of the observed cross sections between $E_x = 0$ and 10 MeV ($\sum_{E_x=0}^{10\ \rm MeV} \sigma_{L=0}^{MD}(\theta)$). As the program DW81 generates DWIA angular distribution down to $\theta = 0°$, the curve had to be extrapolated to $q = 0$ in order to obtain $\sigma(q = 0)$. This was done by setting the Q value for the reaction equal to zero and running the program to get the shape of the curve from $q = 0$ to $q(\theta = 0)$.

In Fig. 9 we show the energy distribution of GT strengths from the MD analysis of the present 130-MeV ^{32}S$(n,p)^{32}$P data, the calculated GT strengths from the OXBASH, the GT analysis of the 135-MeV ^{32}S$(p,n)^{32}$Cl data [7], and the RPA calculation. In this figure, all GT strengths are shown with a full width at half maximum $\Gamma = 1$ MeV to match the binning size of the decomposed (n,p) spectrum. We find an exceptionally good agreement among all four spectra. When a GT transition operator that is consistent with the beta decay of the free neutron, i.e., $g_{\rm free}$, is used in the full s-d model space characterized by Wildenthal's matrix elements [37], a value $\sum_{E_x=0}^{20\ \rm MeV} B(\rm GT) = 3.942$ is obtained (96.2% of which is concentrated below $E_x = 10$ MeV). If the renormalized beta-decay operator of Brown and Wildenthal is

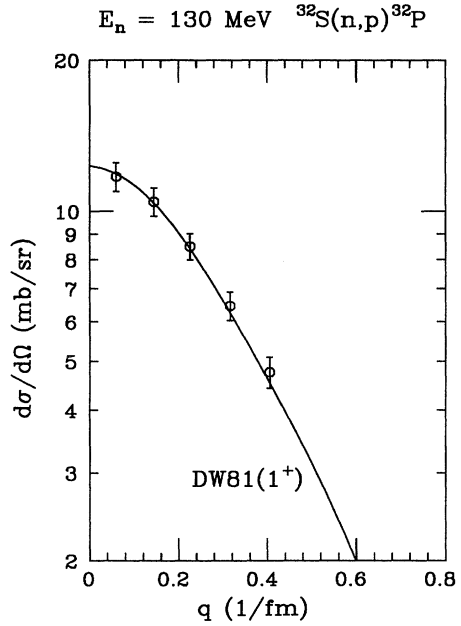

FIG. 8. Sum of GT cross sections for E_x between 0 and 10 MeV from the 130-MeV ^{32}S$(n,p)^{32}$P data as a function of momentum transfers. The curve represents an arbitrarily normalized angular distribution $\sigma(\theta)$ from a DW81 calculation for $J^\pi = 1^+$ at $E_x = 5$ MeV. The shape of the measured angular distribution of the GT cross sections is very well described by the curve.

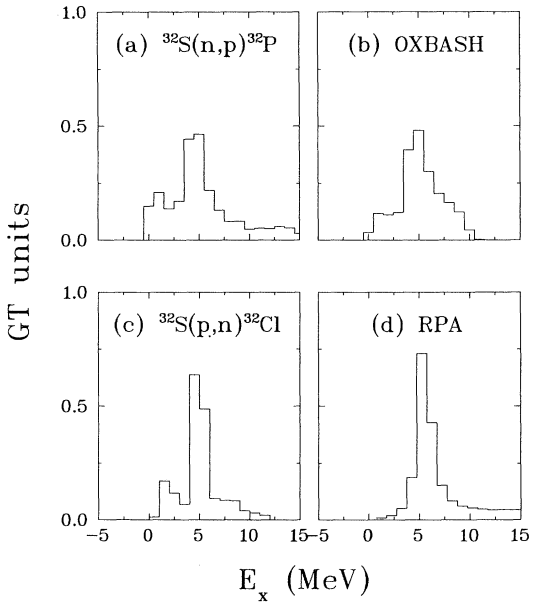

FIG. 9. GT strengths from the MD-analyzed 130-MeV ^{32}S$(n,p)^{32}$P data, OXBASH calculation, the 135-MeV ^{32}S$(p,n)^{32}$Cl data [7], and RPA calculation. Both OXBASH and RPA results have been normalized with $g_{\rm eff} = 0.73$ (see text). In this figure, all GT strengths are shown with a full width at half maximum $\Gamma = 1$ MeV energy resolution to match the binning size of the decomposed (n,p) spectrum.

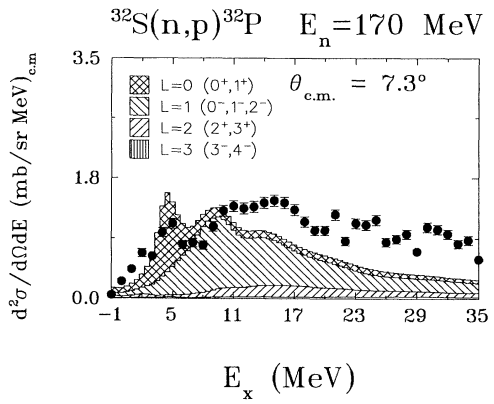

FIG. 10. 170-MeV ^{32}S$(n,p)^{32}$Cl data at $\theta_{\rm c.m.} = 7.3°$ overlaid on the result of the RPA-DWIA calculation.

used [26], i.e., $g_{\rm eff} = 0.73$, then a value $\sum_{E_x=0}^{20\ \rm MeV} B({\rm GT}) = 3.942 \times (0.73)^2 = 2.10$ is predicted. This renormalization value has been obtained in the calculations to reproduce the magnitudes of the beta-decay empirical B(GT) values for s-d shell nuclei. Only when the GT transition operator has been renormalized to produce the observed beta decay B(GT) in the full s-d model space, we observe good agreement in the GT strengths among the OXBASH calculation, RPA calculation also normalized with $(g_{\rm eff})^2 = (0.73)^2 = 0.53$, the (n,p) data, and the (p,n) data.

Below 10 MeV in excitation, we have learned from the MD analysis on the ^{32}S$(n,p)^{32}$P data that about 85% of the GT strength is observed when compared with the GT strength observed in the ^{32}S$(p,n)^{32}$Cl reaction at $E_p = 135$ MeV. However, both the (p,n) and (n,p) results *estimate* roughly the same uncertainties of ± 15%, and the discrepancy found between the two measurements falls in this range of uncertainty. At higher excitation energy region ($10 \le E_x \le 20$ MeV), the MD analysis identifies more GT strength with much the same uncertainty assigned to the GT strength below 10 MeV in excitation. In contrast, the GT strength above 10 MeV in excitation in the ^{32}S$(p,n)^{32}$Cl data analysis *yields* much larger uncertainty which precludes any meaningful discussion in this excitation energy region. The calculations that we have done to obtain the GT strength with the OXBASH and RPA produce very similar outputs as can be seen in Fig. 9.

E. Dipole strength distribution in the ^{32}S$(n,p)^{32}$P reaction

Negative-parity states in ^{32}P, i.e., $1\hbar\omega$ excitations, have not been observed below $E_x = 3.0$ MeV [34]. The present MD analyses of the 95-, 130-, and 170-MeV ^{32}S$(n,p)^{32}$P data are consistent with this observation, as can be seen in Figs. 4, 5, and 6. All $1p$-$1h$ configurations below $E_x = 3.264$ MeV give rise to positive-parity transitions.

Results of the RPA-DWIA calculations for the 170-MeV ^{32}S$(n,p)^{32}$P reaction at $\theta_{\rm c.m.} = 7.3°$ are shown in Fig. 10. The calculated $L = 1$ cross sections are about 60% of the MD-analyzed data. The calculation included all states up to 50 MeV in the continuum; therefore, we cannot attribute the difference in cross sections between the calculations and observed to the presence of the quasifree cross sections. However, it should be mentioned that the position of the dipole peaks in the calculations is sensitive to the single-particle energies.

In Fig. 11 we present the RPA-calculated $L = 1$ cross sections overlaid on the $L = 1$ cross section from the MD-analyzed ^{32}S$(n,p)^{32}$P data at $q \sim 0.5$ fm^{-1}. In this figure, the $L = 1$ cross section calculated with the RPA DWIA is shown with a solid line; a dotted line for $\Delta J^\pi = 0^-$, a dot-dashed line for $\Delta J^\pi = 1^-$, and a dashed line

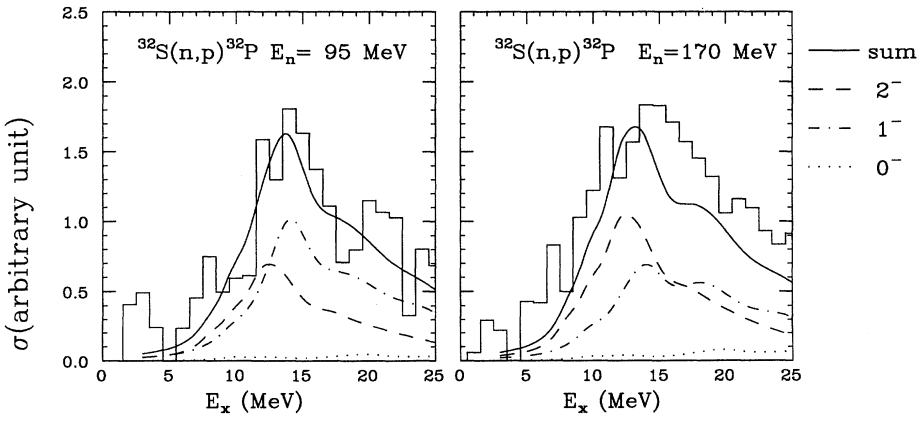

FIG. 11. RPA-calculated $L = 1$ cross sections are overlaid on the $L = 1$ cross section from the MD-analyzed ^{32}S$(n,p)^{32}$P data. The $L = 1$ cross section calculated with the RPA DWIA is shown with a solid line: dotted line for $\Delta J^\pi = 0^-$, dot-dashed line for $\Delta J^\pi = 1^-$, and dashed line for $\Delta J^\pi = 2^-$. The RPA-DWIA $L = 1$ cross sections are shifted +3 MeV and multiplied by 1.6 to match the MD-analyzed (n,p) data.

for $\Delta J^{\pi} = 2^{-}$. The RPA-DWIA $L = 1$ cross sections are shifted +3 MeV and multiplied by 1.6 to match the MD-analyzed (n,p) data. The calculated 2^{-} strength representing the largest component of the GSDR increases with E_n. This feature is very well documented empirically as shown in Fig. 1. As the neutron energy increases above 110 MeV, we observe the GSDR to have a very distinct peak that is well separated from the GDR. On a relative scale, the upper excitation energy region ($E_x \geq$ 12 MeV) is more strongly populated at the lower neutron beam energies than the lower excitation energy region. This also can be seen in Figs. 4 and 6 between the 95 and 170 MeV ^{32}S$(n,p)^{32}$P spectra. Thus, the data indicate good agreement with the energy dependence of the isospin and spin isospin terms of the isovector effective interaction [14].

The GDR is uniquely excited in the photonuclear reaction [38], while the GSDR has been studied with the (e,e') reaction [39]. For qualitative comparisons, we present in Fig. 12 the arbitrarily normalized GDR$^{(\gamma,n)}$ and GSDR$^{(e,e')}$ spectra superimposed on our MD-analyzed $L = 1$ cross sections from $E_n = 95$ and 170 MeV at $\theta_{\rm lab} = 11°$ and $\theta_{\rm lab} = 9°$, respectively. The MD-analyzed $L = 1$ cross section extracted from the 95 MeV ^{32}S$(n,p)^{32}$P data look very much like the GDR$^{(\gamma,n)}$ in

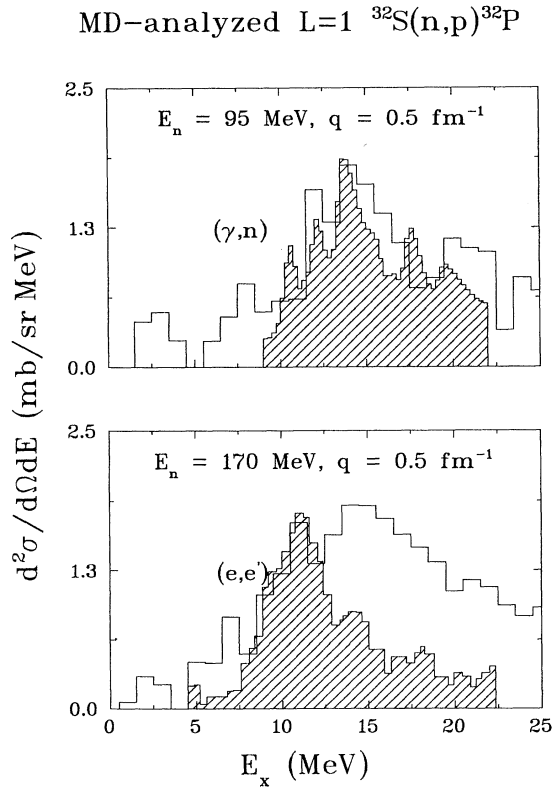

FIG. 12. Qualitative comparison of the MD-analyzed 95 MeV (170 MeV) ^{32}S$(n,p)^{32}$P data at $q \sim 0.5$ fm^{-1} and GDR (GSDR) from (γ,n) [(e,e')] data. Arbitrarily normalized GDR$^{(\gamma,n)}$ and GSDR$^{(e,e')}$ spectra are superimposed on the present (n,p) results. Both the GDR$^{(\gamma,n)}$ and GSDR$^{(e,e')}$ are shifted by -7 MeV in E_x.

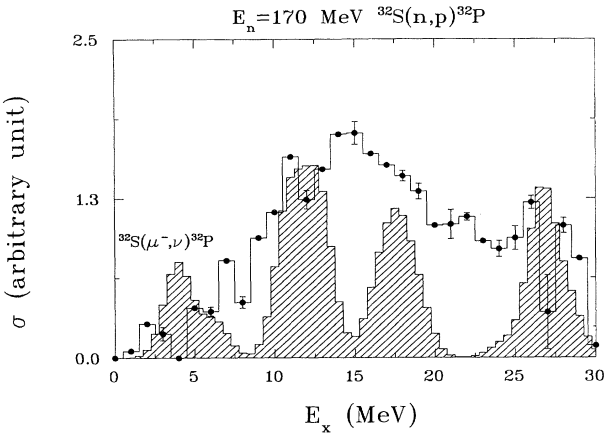

FIG. 13. Calculated dipole excitation spectrum for the (μ^{-},ν) reaction on ^{32}S [40]. The μ capture is represented using a histogram with $\Gamma = 1$ MeV, and the dark circles with error bars represent the ^{32}S$(n,p)^{32}$P data.

the excitation energy region between 10 and 20 MeV. Although small the obvious presence of excitation of some spin-dipole states in the data should account for the difference found in the $E_x = 5$–10 MeV region. We also observe a good agreement between the ^{32}S(n,p) spectrum at 170 MeV and the spin-dipole spectrum from the ^{32}S(e,e') reaction at 200 MeV [39]. A fair amount of the GDR cross section at higher excitation energy is present at this energy. These comparisons help support the argument that a considerable portion of the dipole strength at lower beam energies is from the GDR, whereas the GSDR is more prominent at higher beam energies.

One calculation with which we can compare the present $L = 1$ cross-section values obtained from the MD analysis

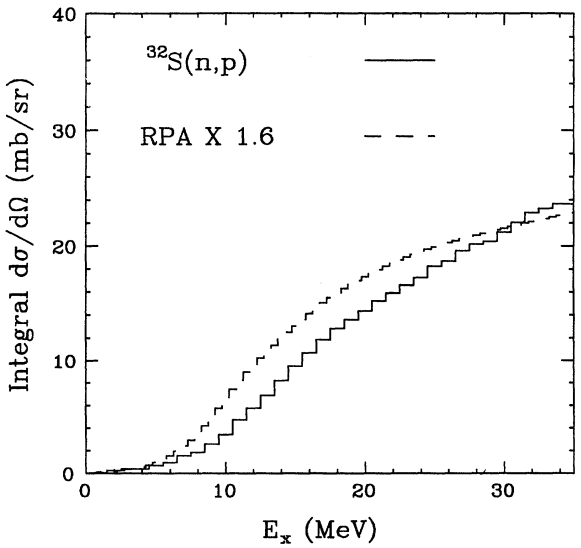

FIG. 14. Integrated sum of the $L = 1$ cross sections from the multipole decomposed spectrum of the 170-MeV ^{32}S$(n,p)^{32}$P data and RPA-DWIA calculations shown in solid and dashed lines, respectively.

is the dipole calculation reported for the $^{32}S(\mu^-,\nu)^{32}P$ reaction [40]. The μ capture on ^{32}S proceeds through the excitation of the giant spin-dipole resonance [39]. In Fig. 13 we present an arbitrarily normalized excitation spectrum for μ capture in ^{32}S overlaid on the multipole decomposed $L = 1$ spectrum for the 170-MeV $^{32}S(n,p)^{32}P$ data. The calculated μ-capture cross section plotted with $\Gamma = 1$ MeV energy resolution resembles, in most part, the multipole decomposed $L = 1$ spectrum.

In Fig. 14 we present the integrated sum of the $L = 1$ cross section from the RPA-DWIA calculations and the MD-analyzed integrated sum cross section for the 170-MeV $^{32}S(n,p)^{32}P$ data, shown in dashed and solid lines, respectively. Magnitude of the calculated cross sections are normalized to the MD-analyzed $L = 1$ cross section. A reasonable agreement in shape is found between the integrated $L = 1$ cross sections of the observed and the RPA-DWIA calculations.

IV. CONCLUSIONS

Double differential cross-section angular distributions were measured for the $^{32}S(n,p)^{32}P$ reaction with a multitarget array and a spallation neutron source. With a proton detection "wall" made of 15 CsI detectors, simultaneous measurements over the incident neutron energies between 60 and 220 MeV covering a reaction angular range of $0° \leq \theta_{lab} \leq 14°$ were carried out.

Excellent agreement was found when the mapped GT transitions in the $^{32}S(n,p)^{32}P$ reaction as a function of (E_n,θ) were compared with those from (p,n) studies and with RPA calculations as well as theoretical calculations done by Brown and Wildenthal [26]. The RPA-DWIA calculation was done to sort out the spin-flip and non-spin-flip contributions to the $L = 1$ excitations. The calculated $L = 1$ cross section is about 60% of the MD-analyzed; however, the integrated cross section seems to match the experimental data in shape.

ACKNOWLEDGMENTS

The authors wish to thank Professor B.A. Brown for his help in running the shell-model code OXBASH. This project was supported in part by the National Science Foundation via Grants Nos. PHY-88-1020-03, PHY-87-22008, and PHY-91-08036, and the U.S. Department of Energy under Contracts Nos. W-7405-ENG-36, DE-AC05-76ER01067, and the Alexander von Humboldt-Foundation.

[1] C. D. Goodman *et al.*, Phys. Rev. Lett. **44**, 1755 (1980).
[2] F. Petrovich, Nucl. Phys. **A354**, 499c (1981).
[3] J. Rapaport, in *Fundamental Symmetries and Nuclear Structure*, edited by J.N. Ginocchio and S.P. Rosen (World Scientific, Singapore, 1988), p. 186.
[4] C.D. Goodman *et al.*, Phys. Rev. Lett. **54**, 877 (1985).
[5] T.N. Taddeucci *et al.*, Nucl. Phys. **A469**, 125 (1987).
[6] F.P. Brady *et al.*, Phys. Rev. Lett. **48**, 860 (1982).
[7] B.D. Anderson *et al.*, Phys. Rev. C **36**, 2195 (1987).
[8] M.A. Moinester, Can. J. Phys. **65**, 660 (1987).
[9] B.K. Park, Ph.D. dissertation, Ohio University, 1991 (unpublished); Los Alamos National Laboratory Report No. LA-UR-91-4136, 1991.
[10] R. Schaeffer and J. Raynal, computer code DWBA70, Arizona State University, 1970 (unpublished); extended version: J.R. Comfort, computer code DW81, Arizona State University, 1984 (unpublished).
[11] B.A. Brown *et al.*, The Oxford-Buenos Aires-MSU Shell-Model Code OXBASH, Michigan State University Cyclotron Laboratory Report No. 524, 1986.
[12] D.J. Rowe, *Nuclear Collective Motion* (Methuen, London, 1970); P. Ring and P. Schuck, *The Nuclear Many-Body Problem* (Springer, New York, 1980); J. Speth, E. Werner, and W. Wild, Phys. Rep. **33**, 127 (1977); D.J. Thouless, Nucl. Phys. **21**, 225 (1960).
[13] N. Auerbach and A. Klein, Phys. Rev. C **30**, 1032 (1984); **28**, 2075 (1983); Nucl. Phys. **A395**, 77 (1983).
[14] M.A. Franey and W.G. Love, Phys. Rev. C **31**, 488 (1985).
[15] D.S. Sorenson *et al.*, Phys. Rev. C **45**, R500 (1992).
[16] P.W. Lisowski *et al.*, Nucl. Sci. Eng. **106**, 208 (1990).
[17] J.L. Ullmann *et al.* (unpublished).
[18] D.S. Sorenson, Ph.D. dissertation, University of California, Davis, 1990; Los Alamos National Laboratory Report No. LA-12061-T, 1991.
[19] R.S. Henderson *et al.*, Nucl. Instrum. Methods A **257**, 97 (1987).
[20] B.K. Park *et al.*, Phys. Rev. C **45**, 1791 (1992).
[21] A.G. Ling *et al.*, Phys. Rev. C **44**, 2794 (1991).
[22] R.A. Arndt and L.D. Roper, Scattering Analysis Interactive Dial-in (SAID) program (SM88) (unpublished); Richard A. Arndt, L. David Roper, Ron L. Workman, and M. W. McNaughton, Phys. Rev. D **45**, 3995 (1992).
[23] B.K. Park, Ohio University Report No. OU91-Accel-01, 1991 (unpublished).
[24] P. Schwandt *et al.*, Phy. Rev. C **26**, 55 (1982).
[25] G.F. Bertsch, *The Practitioner's Shell-Model* (North-Holland, Amsterdam, 1972); M. Carchidi, B.H. Wildenthal, and B.A. Brown, Phys. Rev. C **34**, 2280 (1986).
[26] B.A. Brown and B.H. Wildenthal, Phys. Rev. C **28**, 2397 (1983).
[27] D.J. Millener and D. Kurath, Nucl. Phys. **A255**, 315 (1975).
[28] W. Unkelbach, Ph.D. thesis, University of Bonn, Jül-2477, 1991; H. Condé *et al.*, Nucl. Phys. **A545**, 785 (1992); F. Osterfeld, Rev. Mod. Phys. **64**, 491 (1992).
[29] A.H. Wapstra and G. Audi, Nucl. Phys. **A432**, 1 (1985).
[30] P.M. Endt, Nucl. Phys. **A521**, 1 (1990).
[31] L.D. Landau, JETP **3**, 920 (1957); **5**, 101 (1957); *ibid.* **8**, 70 (1959); A.B. Migdal, *Theory of Finite Fermi Systems and Applications to Atomic Nuclei* (Wiley, New York, 1967); Nucl. Phys. **13**, 655 (1959).
[32] P.D. Kunz, computer code DWUCK4 (unpublished); modified version: W. Unkelbach, 1993 (unpublished).
[33] R.D. Smith and J. Wambach, Phys. Rev. C **38**, 100, (1988); S. Drożdż, S. Nishizaki, J. Speth, and J. Wambach, Phys. Rep. **197**, 1 (1990).
[34] P.M. Endt and C. Van Der Leun, Nucl. Phys. **A310**, 1

(1978).
[35] D.S. Sorenson *et al.*, Phys. Rev. C **45**, R500 (1992).
[36] J. Rapaport, in *Spin and Isospin in Nuclear Interactions*, edited by S.W. Wissink *et al.* (Plenum, New York, 1991), p. 433.
[37] B.H. Wildenthal, Prog. Part. Nucl. Phys. **11**, 5 (1984); additional information on techniques can be found in B.H. Wildenthal, M.S. Curtin, and B.A. Brown, Phys. Rev. C **28**, 1343 (1983).
[38] D.V. Webb *et al.*, Phys. Rev. **164**, 1397 (1967).
[39] R.A. Eramzhyan *et al.*, Phys. Rep. **136**, 229 (1986).
[40] Yu.I. Bely and N.M. Kabachnik, Yad. Fiz. **14**, 1113 (1971); Yu.I. Bely *et al.*, Nucl. Phys. **A204**, 357 (1973).